On Frequency-dependent Dispersion Measures and Extreme Scattering Events

M. T. Lam[1,2,3,4] , T. J. W. Lazio[5], T. Dolch[6] , M. L. Jones[7] , M. A. McLaughlin[7] , D. R. Stinebring[8] , and M. Surnis[7]

[1] School of Physics and Astronomy, Rochester Institute of Technology, Rochester, NY 14623, USA; michael.lam@mail.wvu.edu
[2] Laboratory for Multiwavelength Astronomy, Rochester Institute of Technology, Rochester, NY 14623, USA
[3] Department of Physics and Astronomy, West Virginia University, White Hall, Morgantown, WV 26506, USA
[4] Center for Gravitational Waves and Cosmology, West Virginia University, Chestnut Ridge Research Building, Morgantown, WV 26505, USA
[5] Jet Propulsion Laboratory, California Institute of Technology, 4800 Oak Grove Drive, Pasadena, CA 91109, USA
[6] Department of Physics, Hillsdale College, 33 E. College Street, Hillsdale, MI 49242, USA
[7] Department of Physics and Astronomy, West Virginia University, P.O. Box 6315, Morgantown, WV 26506, USA
[8] Department of Physics and Astronomy, Oberlin College, Oberlin, OH 44074, USA

Abstract

Radio emission propagating over an Earth-pulsar line of sight provides a unique probe of the intervening ionized interstellar medium (ISM). Variations in the integrated electron column density along this line of sight, or dispersion measure (DM), have been observed since shortly after the discovery of pulsars. As early as 2006, frequency-dependent DMs have been observed and attributed to several possible causes. Ray-path averaging over different effective light-cone volumes through the turbulent ISM contributes to this effect, as will DM misestimation due to radio propagation across compact lensing structures such as those caused by "extreme scattering events (ESEs)." We present methods to assess the variations in frequency-dependent DMs due to the turbulent ISM versus these compact lensing structures along the line of sight. We analyze recent Low-Frequency Array observations of PSR J2219+4754 to test the underlying physical mechanism of the observed frequency-dependent DM. Previous analyses have indicated the presence of strong lensing due to compact overdensities halfway between the Earth and pulsar. Instead, we find the frequency dependence of the DM time series for PSR J2219+4754 is consistent with being due solely to ISM turbulence and there is no evidence for any ESE or small-scale lensing structure. The data show possible deviations from a uniform turbulent medium, suggesting that there may be an enhanced scattering screen near one of the two ends of the line of sight. We present this analysis as an example of the power of low-frequency observations to distinguish the underlying mechanisms in frequency-dependent propagation effects.

Unified Astronomy Thesaurus concepts: Radio pulsars (1353); Interstellar medium (847); Interstellar plasma (851); Pulsar timing method (1305)

1. Introduction

The propagation of radio pulsar emission through the interstellar medium (ISM) provides a unique probe of ionized material along the path of propagation (Rickett 1990). Estimates of the dispersion measure (DM), or integrated electron column density, are obtained from precisely measuring the arrival times of pulse emission as a function of radio frequency (Stairs 2002). Measurements of how these dispersive delays, along with other frequency-dependent delays, change over time allow us to build models of structures in the ISM on a wide range of spatial scales (Armstrong et al. 1995).

While temporal DM variations have been observed for decades (Rankin & Roberts 1971; Phillips & Wolszczan 1991, 1992; Backer et al. 1993; Hobbs et al. 2004), frequency-dependent DM due to differing volumes of the ISM probed has only been observed more recently, e.g., for PSR B1937+21 in Ramachandran et al. (2006) and Demorest (2007); see also Pennucci (2015). A thorough treatment on the theory of frequency-dependent DM was given by Cordes et al. (2016). Ray-path averaging of the radio emission through different volumes—and therefore different electron content—of the turbulent ISM will result in a smoothing of the DM time series by a kernel that broadens rapidly at lower frequencies.

Besides dispersive delays, there are a number of other physical mechanisms that cause the propagating radio emission to be delayed. These delays vary as a function of frequency (Foster & Cordes 1990; Clegg et al. 1998; Shannon & Cordes 2017). One example is from lensing of the emission around compact over- or underdensities in the ISM (Clegg et al. 1998; Cordes et al. 2017). However, since typical pulsar timing models only account for dispersive delays, there will be errors associated with the estimated DM due to these additional delays (Cordes & Shannon 2010; Lam et al. 2016b). Therefore, DM estimates taken at two separate frequencies may show differences solely due to biases from these other propagation effects and can be misattributed to a frequency dependence in the true dispersive delay.

Donner et al. (2019) have most recently reported three-and-a-half years of timing measurements of PSR J2219+4754 (B2217+47) with three stations of the International LOFAR (LOw-Frequency ARray) Telescope (ILT). From those data, they have determined frequency-dependent variations in the DM. The temporal variations noted in the DM time series for PSR J2219+4754 for both the lower- and higher-frequency data qualitatively appear very similar to those predicted by Cordes et al. (2016) for a turbulent medium, especially in that the higher radio-frequency DM data show higher fluctuation/Fourier-frequency structure than the lower radio-frequency time series. Donner et al. (2019) concluded, however, that while the data are consistent with arising from the turbulent medium, the DM variations result from small-scale (∼1 au) structure(s) in the ISM, potentially multiple extreme scattering events (ESEs).

ESEs were originally seen as localized "events" in flux density measurements of compact radio sources (Fiedler et al. 1987; Cognard et al. 1993; Maitia et al. 2003). The first

measurements of ESEs observed in DM and scintillation/scattering measurements were performed by Coles et al. (2015), who described ESEs observed toward two pulsars.

This line of sight is particularly unique due to observed "light echoes" in the trailing components of the pulsar's pulse profile (Michilli et al. 2018) using LOFAR. These additional components were seen to vary with time. Michilli et al. (2018) described several possible mechanisms, with one requiring the lensing of radio emission due to passage near a compact interstellar structure, like those causing ESEs. Such lensing would cause the emission to traverse slightly different paths through the ISM, which could manifest as some combination of dispersive delays and light-travel-time delays. Given the complexity of the observed features, the line of sight toward PSR J2219+4754 therefore represents an excellent laboratory to test the predictions of Cordes et al. (2016) to disentangle the properties of the intervening medium.

In this work, using the data on PSR J2219+4754 as a test to distinguish between the different physical mechanisms, we carry out analyses to determine whether or not the observations are consistent with lensing events or with the theoretical expectation from a turbulent medium. In Section 2, we build upon their structure-function analysis to show consistency of the frequency-dependent DM with the theoretical predictions for a Kolmogorov medium in Cordes et al. (2016). In Section 3, we further examine the reported ESE detection, analyzing the impact of a variety of timing effects on their results. We apply a wide range of analyses discussed in the literature to understanding this specific line of sight, including: (i) determining the probability for the false signature of a gradient to be seen in the DM time series; (ii) establishing the importance of the solar wind on the frequency-dependence of DM and testing if a DM gradient is due to the changing Earth–pulsar line of sight; (iii) determining the impact of nondispersive delays on DM estimation, specifically the amplitude of the delay caused by refraction from a lensing structure; (iv) understanding the systematic bias of pulse profile evolution in both time and frequency on these analyses; (v) accounting for various components of pulse arrival-time uncertainties, demonstrating the importance of high-precision pulsar timing techniques given the sensitivity of the measurements; (vi) developing a method built upon traditional structure function analyses, providing a more robust measure of the expected amplitude of the frequency-dependent DM while further showing inconsistencies with gradients in the DM time series; and (vii) implementing this structure function method on the data presented in Donner et al. (2019) in order to gain additional insights regarding the line of sight. We found through our analyses that any lensing structure as described by Donner et al. (2019) would affect the various observables in a way that has not been seen, thereby ruling out such a structure. We discuss the impact on precision pulsar-timing experiments in Section 4 and briefly discuss possible future observations of this type in Section 5. In the Appendix, we provide a derivation for DM estimation errors in the presence of time-of-arrival (TOA) uncertainties and additional frequency-dependent time delays that is useful for a number of arguments in our work.

2. Structure Function Analysis and Frequency-dependent DM

Structure functions are used in analyses of pulsar DM time series, as well as the broader literature on turbulence in general,

as a method of constraining the spectral properties of the variations (Cordes & Rickett 1998). From the structure function, one can derive the amplitude of the electron-density wavenumber spectrum, which directly relates to the size of the fluctuations seen in DM time series (Rickett 1990). Therefore, they can also be used to quantify the magnitude of the differences between DM time series measured at two frequencies (Cordes et al. 2016). The variations in the observations presented in Donner et al. (2019) provide a strong data set with which to test for the root-mean-square (rms) fluctuations in the DM differences with both frequency and time.

As part of their analysis, Donner et al. (2019, see their Figure 6) determined the structure function of the DM(t) time series, defined as $D_{\mathrm{DM}}(\tau) = \langle [\mathrm{DM}(t + \tau) - \mathrm{DM}(t)]^2 \rangle$, where τ is the time lag separating two observations and the brackets denote the ensemble average. The authors found a power-law structure function with a spectral index consistent with that of Kolmogorov turbulence. The fit was performed over lags $\tau \leqslant 200$ days. Note that the calculated structure function shows clear evidence of a white noise contribution at lags $\tau \lesssim 30$ days. A white noise contribution to a time series will produce a "plateau" at small lags (e.g., Cordes & Downs 1985) or for any trends (e.g., linear) in the data (Lam et al. 2016b; Jones et al. 2017) and bias the fit for the spectral index, which will itself become a function of τ. For the purposes of this paper, we accept that a Kolmogorov (or near-Kolmogorov) spectrum is an acceptable fit to the DM structure function given the clear overlap with the estimated values shown. We will assume from here that the spectrum is described by a Kolmogorov medium, based on the observed consistency with this model in the ISM (e.g., Armstrong et al. 1995).

Following the determination of a Kolmogorov spectrum, the authors then concluded that the cause of the variations may be due to ESEs, which they describe in a context other than localized events. A spectrum steeper than Kolmogorov or discrete structures (or both) are required to produce ESEs and the refractive effects observed in pulsar dynamic spectra (e.g., Roberts & Ables 1982; Hewish et al. 1985; Cordes & Wolszczan 1986; Romani et al. 1987). The turbulence in the ISM is often described with an electron-density wavenumber spectrum having a power-law form (see, e.g., Armstrong et al. 1995)

$$P_{\delta n_{\mathrm{e}}} = C_n^2 q^{-\beta}, \quad q_1 \leqslant q \leqslant q_2, \qquad (1)$$

where $q = 2\pi/l$ is the wavenumber corresponding to physical scale l and C_n^2 is the spectral coefficient representing the overall amplitude or strength of the turbulence. The low and high wavenumber cutoffs represent outer and inner physical scales, respectively. A Kolmogorov medium corresponds to $\beta = 11/3$. Strong refractive effects occur for a density spectral index $\beta > 4$ (Cordes et al. 1986), which was not observed for PSR J2219+4754. Notably, Donner et al. (2019) referenced Fiedler et al. (1994) and Coles et al. (2015) as examples of ESEs in which larger-scale turbulent structure is identified as the cause of the observed lensing; however, both of those works instead find the causes of their observations to be due to structures consistent with compact canonical ESEs, i.e., smaller-scale lenses as described previously in the literature and above. In the former, the authors did examine the associated large-scale structure of the ISM in the foreground of sources with observed ESEs from

Fiedler et al. (1987). In the latter, the outer scale of the ESE was taken to be on the order of the size scale of the smallest dimension of the lens, which is distinct from the outer scale of the electron-density wavenumber spectrum of the ionized ISM written above, known to be many orders of magnitude larger (Armstrong et al. 1995).

Using the constant value of the amplitude of the wavenumber spectrum Donner et al. (2019) estimated, $C_n^2 = 0.9 \times 10^{-3}$ m$^{-20/3}$, and a distance estimate of 2.2 kpc from the NE2001 electron density model (Cordes & Lazio 2002), the corresponding scattering measure is SM $= \int_0^{D_p} C_n^2(z)\,dz = 2.0 \times 10^{-3}$ kpc m$^{-20/3}$, an order of magnitude higher than the value predicted by the NE2001 model.[9] Following Cordes et al. (2016, see Equation (12)), the rms difference in DM between two spot frequencies ν_1 and ν_2, where $\nu_1 < \nu_2$, for a uniform Kolmogorov medium is

$$
\sigma_{\mathrm{DM}(\nu)}(\nu_1, \nu_2) = 3.76 \times 10^{-5} \ \mathrm{pc \ cm^{-3}} \ F_{11/3}(r)\left(\frac{G_{11/3}}{0.145}\right)
$$
$$
\left(\frac{D_p}{1 \ \mathrm{kpc}}\right)^{5/6} \times \left(\frac{\nu_2}{1 \ \mathrm{GHz}}\right)^{-11/6} \left(\frac{\mathrm{SM}}{10^{-3.5} \ \mathrm{kpc \ m^{-20/3}}}\right),
$$
$$
(2)
$$

where the frequency ratio $r \equiv \nu_2/\nu_1$, $F_{11/3}(r)$ is a factor that contains all of the relative frequency dependence (Cordes et al. 2016, see Equation (11)), $G_{11/3}$ is a geometric-only factor where the fiducial value of 0.145 is for a uniform Kolmogorov medium (Cordes et al. 2016, see Table 1), and D_p is the pulsar distance. For frequencies at the centers of the two frequency bands from the observations of Donner et al. (2019), we have $\sigma_{\mathrm{DM}(\nu)}(133 \ \mathrm{MHz}, 169 \ \mathrm{MHz}) = 0.6 \times 10^{-3}$ pc cm^{-3}, while for the extremes of the bands, $\sigma_{\mathrm{DM}(\nu)}(118 \ \mathrm{MHz}, 190 \ \mathrm{MHz}) = 1.1 \times 10^{-3}$ pc cm^{-3}. The bottom panel of Figure 5 of Donner et al. (2019) shows rms variations at exactly these levels, suggesting that the observed frequency-dependent DM is consistent with the theoretical predictions of Cordes et al. (2016) for a Kolmogorov medium.

3. Testing the ESE Interpretation

Frequency-dependent DM results from ray-path averaging over different volumes of the intervening medium. Refraction by discrete structures along the propagation path can also result in variations in DM time series via misestimation from nondispersive delays (Foster & Cordes 1990; Cordes et al. 2017). These delays can therefore be useful in characterizing such discrete structures (e.g., Lam et al. 2018a). However, care needs to be taken in order to properly account for all effects in timing data.

Following their analysis of the structure function, Donner et al. (2019) proposed an interpretation of the DM variability due to plasma lensing structures. For simplicity, they made an assumption that the variability is due to one to three spherical lenses. Under this assumption, they found the potential parameters of one of the clouds (see their Figure 7). In this section, we will present an alternative explanation from a lens

as described by Donner et al. (2019) via characterization of the pulse arrival times in conjunction with the DM time series.

Qualitatively, the appearance of the DM time series is similar to that of other pulsars; for example, in the DM time series presented by Jones et al. (2017), one can identify similar features for PSR J0613−0200, PSR B1937+21, and potentially other pulsars in that data set alone.

Evidence of these features being caused by something other than ESEs can be found by considering the expected DM amplitude. Donner et al. (2019) identified the variation in DM between MJD 56950 and 57100 (their Figure 1) as an ESE by virtue of its amplitude $|\delta\mathrm{DM}| \approx 3 \times 10^{-3}$ pc cm^{-3}. By considering their calculated structure function and relating that to the expected rms variations in the DM (Lam et al. 2016b, Equation (30)), we find

$$
\sigma_{\mathrm{DM}}(\tau) = \left[\frac{1}{2}D_{\mathrm{DM}}(\tau)\right]^{1/2}
$$
$$
= 1.2 \times 10^{-5} \ \mathrm{pc \ cm^{-3}}\left(\frac{\tau}{\mathrm{day}}\right)^{5/6}. \qquad (3)
$$

For $\tau = 150$ days, then $\sigma_{\mathrm{DM}}(150 \ \mathrm{days}) = 0.8 \times 10^{-3}$ pc cm^{-3}, and $|\delta\mathrm{DM}|$ is much larger than the expected rms variation.

If the DM variation is from a true steep gradient, then we can use an estimate of the rms DM gradient (rather than the rms DM; Lam et al. 2016b),

$$
\sigma_{d\mathrm{DM}/dt} \approx \frac{\sigma_{\mathrm{DM}}(\tau)}{\tau}, \qquad (4)
$$

and compute the "signal-to-noise" ratio for such a gradient,

$$
R_{d\mathrm{DM}/dt} \equiv \frac{|d\mathrm{DM}/dt|}{\sigma_{d\mathrm{DM}/dt}}. \qquad (5)
$$

Evaluating for $|d\mathrm{DM}/dt| = 2 \times 10^{-5}$ pc cm^{-3} day^{-1}, we find that $R_{d\mathrm{DM}/dt} = 3.8$ over the 150 day duration of the purported ESE, suggesting moderate significance. However, while the DM obtained from analyzing the entire frequency range shows a rising linear trend prior to this time period, in the split-frequency DM time series, the <149 MHz values are consistent with a constant DM within ∼1σ, and therefore there is no apparent ingress into the assumed spherically symmetric lensing material for those frequencies. Therefore, a canonical ESE interpretation seems unlikely, though a potential DM gradient may still be plausible. Note that the egress time period occurs around MJD 57100, right when the DM difference between the time series is zero by construction. It is thus unclear if this time period truly marks the end of such an event or not.

We investigated whether this potential DM gradient could be due to the line of sight cutting through different parts of the solar wind. By MJD 56950 moving forward, the suggested time of a peak, the solar elongation is shrinking (for reference, the pulsar's ecliptic latitude is 52°.5). Thus, as the pulsar as seen on the sky approaches the Sun, we would expect the DM to increase (only slightly, due to the high ecliptic latitude) rather than decrease (You et al. 2007b; Jones et al. 2017; Madison et al. 2019). Any solar flare or coronal events that may have occurred during this time span would also cause an increase rather than a decrease in the DM (Lam et al. 2016b). In

---

[9] We note this measurement (and an extrapolation to the estimate of the scintillation timescale discussed later) may then be useful in constraining properties in future electron density models or uncovering interesting turbulence physics along this line of sight.
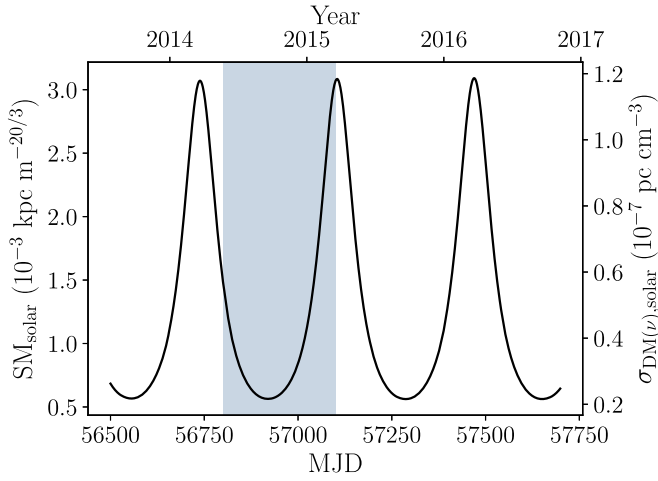
Figure 1. SM due to the solar wind along a line integrating out from the Earth to the direction of PSR J2219+4754. Right axis shows the equivalent $\sigma_{\mathrm{DM}(\nu)}$ uncertainty. Blue shaded region denotes the 300 day time span of the proposed lens.

addition, we looked at the C_n^2 contribution due to turbulence in the solar wind using the form provided in Spangler et al. (2002),

$$C_n^2(r) = 1.8 \times 10^{10} \left(\frac{r}{10\,R_\circ}\right)^{-3.66} \mathrm{m}^{-20/3}, \qquad (6)$$

where r is the radial distance from the Sun. We integrated the solar wind C_n^2 over the line of sight to determine the SM, shown in Figure 1. With each integration element acting as a thin screen, we determined the frequency-dependent DM error and then combined these to find a total error of

$$\sigma_{\mathrm{DM}(\nu),\mathrm{solar}} = \sqrt{\frac{1}{\langle 1/\sigma_{\mathrm{DM}(\nu)}^2(s)\rangle}}, \qquad (7)$$

i.e., the total error is the square root of the reciprocal of the mean of the "weights" ($1/\sigma^2$), and we are integrating along the line-of-sight position s for each volume element. We find that, while the SM is increasing over the time of the suggested ESE and is of a value similar to the rest of the ISM (fiducial value of $10^{-3.5}$; Rickett 1990; Cordes & Rickett 1998)—because the material is very close to the Earth in comparison with the pulsar's distance—the rms frequency-dependent DM is small, well below the measurement uncertainties and even below that of other high-precision timing experiments (see, e.g., Jones et al. 2017).

For variations in DM due to the changing ionosphere, in this case because of the yearly modulation from observing the pulsar transitioning between day and night over that time period, the amplitude of the change in DM is at most $\sim 10^{-4}$ pc cm^{-3} and therefore is not a significant contributor to the variation here (Lam et al. 2016b).

3.1. Impact of Nondispersive Delays

As has been described in the literature, there are multiple frequency-dependent delays that affect pulsar TOAs (Foster & Cordes 1990; Lam et al. 2016b, 2018a; Shannon & Cordes 2017). Beyond the traditional dispersive delay due to the integrated electron density ($\propto \nu^{-2}$), there is a geometric

delay ($\propto \nu^{-4}$) due to total path length changes and a barycentric-correction delay ($\propto \nu^{-2}$) due to the angle of arrival of the pulsar shifting, i.e., the pulsar's image appearing from a different direction on the sky.

Following the notation in Lam et al. (2018a), the dispersive delay for a lens of size L, electron density n_e, and dispersion measure $\mathrm{DM}_l \sim n_e L$, is

$$t_{\mathrm{DM}} \sim \frac{\lambda^2 r_e \mathrm{DM}_l}{2\pi c} \sim \frac{\lambda^2 r_e n_e L}{2\pi c}, \qquad (8)$$

where λ is the electromagnetic wavelength, r_e is the classical electron radius, and c is the speed of light. The geometric delay is

$$t_{\mathrm{geo}} \sim \frac{D_l(1 - D_l/D_p)\lambda^4 r_e^2 (\mathrm{DM}_l')^2}{8\pi^2 c} \sim \frac{D_l(1 - D_l/D_p)\lambda^4 r_e^2 n_e^2}{8\pi^2 c \zeta^2} \qquad (9)$$

where D_l and D_p are the distance to the lens and pulsar (from the observer), respectively, and $\mathrm{DM}_l' \sim n_e L/(\zeta L) \sim n_e/\zeta$ is the DM spatial gradient with the depth-to-length aspect ratio of the lens as ζ. Finally, the barycentric delay is

$$t_{\mathrm{bary}} \sim \frac{(1 - D_l/D_p)\lambda^2 r_\oplus r_e \mathrm{DM}_l'}{2\pi c} \sim \frac{(1 - D_l/D_p)\lambda^2 r_\oplus r_e n_e}{2\pi c \zeta}, \qquad (10)$$

where $r_\oplus$ is the Earth–Sun distance of 1 au.

Following Donner et al. (2019), we assume that the cloud is spherical and therefore we set $\zeta = 1$. The time for the cloud to pass through the line of sight is ~ 300 days. With a proper motion of 22.2 mas yr^{-1} (Michilli et al. 2018), the angle subtended on the sky is $\theta = 18.2$ mas. The angle sets the physical size of the cloud as $L = \theta D_l$. Therefore, the distance of the lens is linearly proportional to the size of the lens (shown by Donner et al. 2019 in the bottom panel of their Figure 7). Given that the DM change from the cloud is simply $n_e L$, we have that n_e is inversely proportional to the cloud size and inversely proportional to the lens distance (shown by Donner et al. 2019 in the top panel of their Figure 7).

The distance estimate for a possible structure in the ISM causing light "echoes" seen in the pulse profiles for PSR J2219 +4754 is $D_l \approx 1.1$ kpc (Michilli et al. 2018), a companion paper to the work of Donner et al. (2019). Using the DM change of $|\delta\mathrm{DM}| \approx 3 \times 10^{-3}$ pc cm^{-3}, Figure 2 shows the dispersive, geometric, and barycentric delays for such a lensing structure at 1.1 kpc. We see that the dispersive delay dominates over the geometric and barycentric delay. However, when fitting the total frequency-dependent delays observed, the estimated infinite-frequency arrival time is shifted from the true arrival time by 93 μs; the estimated DM would then be larger than the $|\delta\mathrm{DM}|$ above by 7.1×10^{-3} pc cm^{-3}, which is unseen in the time series unless the baseline DM value is far lower than suggested by Donner et al. (2019).

In Figure 3, we show the perturbation in t_∞ and DM (the difference between the "true" DM from the dispersive delay and that from the misestimation) after fitting the total delay curve generated by placing a lens at a distance D_l; again, Figure 2 shows the three frequency-dependent delays along with the total delays when $D_l = 1.1$ kpc. These perturbations were calculated after fitting each delay curve with the functional form $t_\nu = t_\infty + K\mathrm{DM}/\nu^2$. For reference, the forms
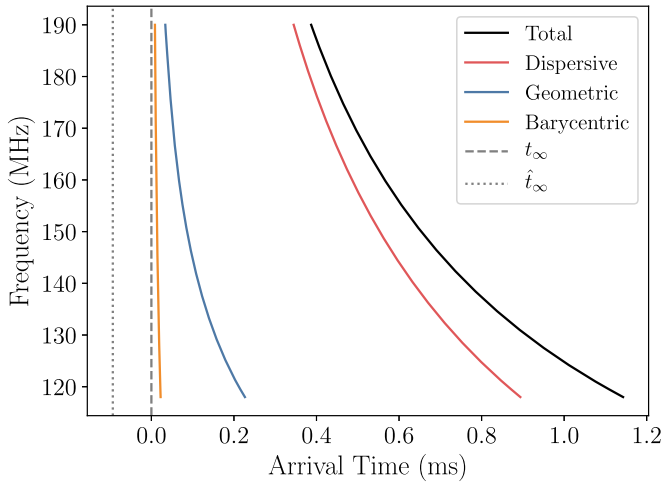
Figure 2. Pulse delays as a function of time and frequency. Total delay is the sum of the dispersive, geometric, and barycentric delays. Dashed gray line shows the true infinite-frequency arrival time (set to zero) while the dotted gray line shows the estimated infinite-frequency arrival time when a purely dispersive delay is fit over all frequencies to the total delay (i.e., extrapolating the delay curve to infinite frequency), $\delta t_\infty = -93\ \mu s$. We assume a cloud 1.1 kpc away from the Earth, the estimate for the distance in Michilli et al. (2018), which implies a size $L = 20$ au and central density $n_e = 31$ cm^{-3} (from our analysis, but also see Figure 7 of Donner et al. 2019). For clarity, the legend from top to bottom displays the different curves from right to left.
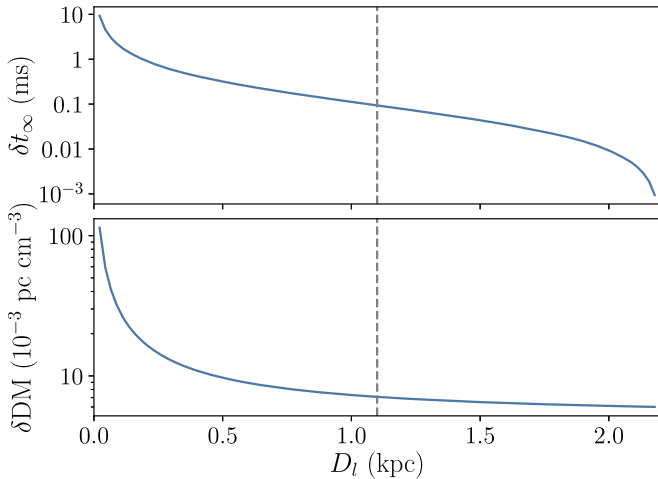

Figure 3. TOA perturbation (top) and DM perturbation (bottom) when fitting for the set of total frequency-dependent delays (e.g., see Figure 2) vs. only the dispersive delay. We display these perturbations as a function of the lens distance.

of these perturbations for two spot frequencies are shown in the Appendix.

If we split the total band into two halves to measure the frequency-dependence of DM, the increases in δDM are then 7.3 and 6.8×10^{-3} pc cm^{-3} for the low and high bands, respectively, or a difference of 5×10^{-4} pc cm^{-3} between the two. This value is approximately half of the difference between the two bands shown by Donner et al. (2019) in their Figure 5. Recall, however, that in this calculation we started with a single DM, and only when estimating the DM in both halves of the band did we recover frequency dependence, solely from the unaccounted for $\propto \nu^{-4}$ geometric delay rather than from a true DM difference. This demonstrates why a complete analysis of
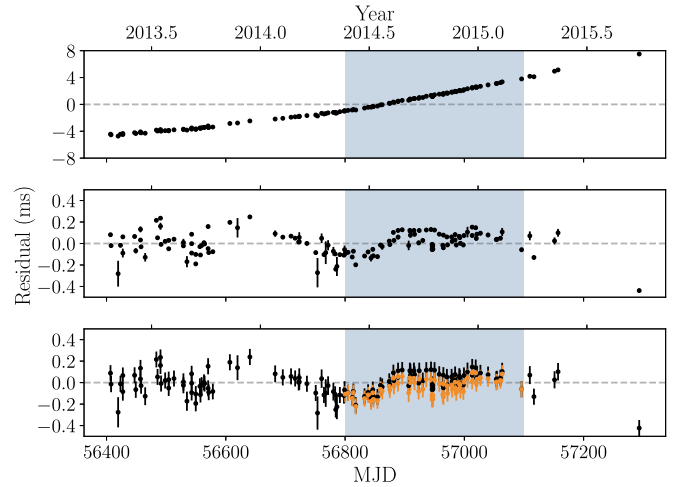

Figure 4. Timing residuals from Michilli et al. (2018). Top: Original residual values as plotted in Michilli et al. (2018), after a fit for spin and astrometric parameters, a mean DM, and one glitch. The steep trend is likely due to longer-term spin noise (Shannon & Cordes 2010). Middle: For visual clarity only, on the scatter of the residuals, we have removed the best-fit quadratic trend. Bottom: In black are the same residuals as shown in the middle panel, but with the contributions of jitter ($\approx 10\ \mu s$) and polarization miscalibration ($\approx 80\ \mu s$) added in quadrature. The quadratic trend was not refitted since it is only used as a visual aid. Blue shaded regions in all panels denote the 300 day time span of the proposed lens. Red points in the bottom panel show the impact of a lens with timing perturbations to t_∞ represented as a triangle function with the amplitude going from 0 to $-93\ \mu s$ in the middle and back to 0.

the arrival times, such as in Lam et al. (2018a), is crucial to understanding any potential lens/ESEs in the data, rather than analyzing only the DM time series.

We examined the long-term timing residuals in (Michilli et al. 2018, see their Figure 1) for PSR J2219+4754 from observations covering 1970 to 2016. Figure 3 shows that the TOA perturbations due to a lens should be on the order of microseconds or greater, depending on the distance, and for a lens at distance 1.1 kpc, we expect a perturbation of ≈ 0.1 ms if $\propto \nu^{-4}$ delays are not fit for. We replot the residuals as directly shown in Michilli et al. (2018) in Figure 4, starting with the earliest observation epoch in Donner et al. (2019). For reference, decimal year 2015.5 corresponds to the end of the time period in which Donner et al. (2019) stated no baseline DM variations were observed. The blue shaded region denotes the 300 day time period over which the proposed lens occurs. In the middle panel, we show the residuals after a quadratic subtraction so that the scatter is more clearly visible. In the bottom panel, we show the same residuals as in the middle but with an increase in the TOA uncertainties due to jitter ($\approx 10\ \mu s$) and polarization miscalibration ($\approx 80\ \mu s$) as described later in Section 3.3. In red, we have injected the systematic effect on the timing given the lens described above, where we simplify input of the offsets as a triangle function starting at 0, decreasing to $-93\ \mu s$ in the middle, and increasing back to 0. Given the scatter in the residuals and the unknown contributions to spin noise, we cannot prove or disprove the presence of a lens at 1.1 kpc. As per Figure 3, a lens closer than 1.1 kpc will show increasingly dramatic dips in the residual time series, which would become readily visible.

Michilli et al. (2018) also showed the evolution of the pulsar's spindown rate. While this curve is also smoothly varying, we see a drop right at the start of 2015 (around

MJD 57000), during the time of the proposed ESE. Donner et al. (2019) indicated that a single spin-period derivative (Michilli et al. 2018 showed the equivalent spin-frequency derivative) was fit in their own timing model. The spindown rate shown in Michilli et al. (2018) was not constant over this time period, suggesting that if the spin-frequency derivative was smaller than the average value in the fit by Donner et al. (2019), then the pulsar's spin was braking more rapidly (i.e., the spin frequency was dropping more rapidly) than expected and the infinite-frequency arrival times should be delayed compared to their model (a linear change would have been absorbed by the shorter-duration fit, but we do not see that either). Any fit for DM would therefore be biased by this effect. Visualized in terms of the delay curves in Figure 2, the true arrival time would be delayed, i.e., shifted to the right.

Rather than investigating the impact on the timing residuals, we directly investigated the impact on the two DM time series. Given the arguments above, if there were an intervening lens with a true column density equal to DM $\approx 3 \times 10^{-3}$ pc cm^{-3} that passed the line of sight, the differences in DM between the two bands could potentially be explained—but not the amplitude change of $\approx 7 \times 10^{-3}$ pc cm^{-3} in the DM time series from the zero value, thereby ruling out a lens with such a column density. It is possible that if a lens with a lower column density were to pass by the line of sight, it would show up with an apparent DM having the appropriate amplitude as estimated by the total time delays. One can search over the phase space of the true column density/DM, size L, and distance D_l to find the best-fit parameters of a possible lens. As stated previously, for a spherically symmetric lens, we would expect the DM time series from both bands to behave symmetrically.

In addition to the three delays described above, general scattering (alternatively, pulse broadening) from a Kolmogorov medium will produce arrival-time delays $\propto \nu^{-4.4}$. Donner et al. (2019) stated that if the frequency-dependent DM is variable in time, then non-ν^{-2} dispersive delays will vary equally in time. From Cordes et al. (2016), we see that the time- and frequency-dependence of DM arises naturally from ray-path averaging over different volumes of the ISM if there is an effective velocity between the Earth, pulsar, and bulk ISM motions (regarding the effective velocity, see Cordes & Rickett 1998). Such variations can arise even for a medium with constant C_n^2, which for example can yield a statistically constant scattering timescale even while the DM varies. Changes in pulsar scattering timescales have been observed (e.g., Coles et al. 2015; Levin et al. 2016), which require a change in C_n^2 (or the inner scale of the turbulence, again see Cordes & Rickett 1998) and therefore the statistics of the DM variations, though the time series of each need not be correlated one-to-one. As with the geometric and barycentric delay, a $\propto \nu^{-4.4}$ scattering delay will also cause DM to be incorrectly estimated if not properly modeled. Donner et al. (2019) noted that unmodeled scattering does affect their results but is small enough in amplitude that it does not change their conclusions substantially.

3.2. Impact of Frequency- and Time-dependent Profile Evolution

The variability of the pulse profile of PSR J2219+4754 with time was discussed in Michilli et al. (2018) in the context of light echoes due to propagation effects. Bilous et al. (2016) showed in an observation taken in early 2014 (around MJD 56700) that there was significant frequency dependence in the
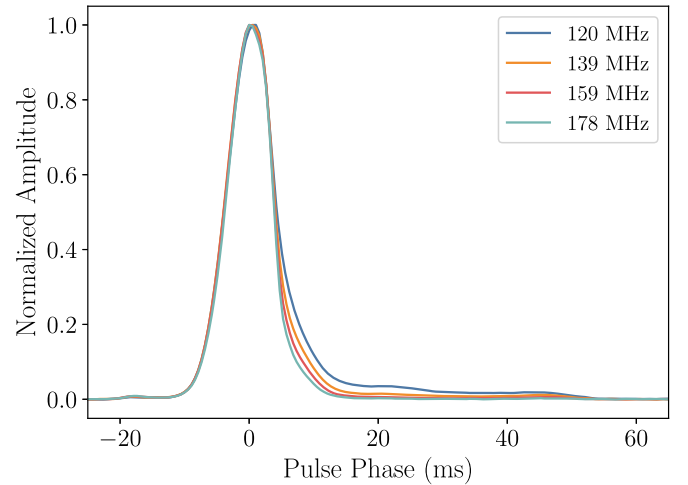

Figure 5. Profiles of PSR J2219+4754 as a function of frequency from Bilous et al. (2016). Pulse phase is centered at the peak and only a small part around the main pulse is shown for clarity.

pulse profile. Using profiles of PSR J2219+4754 from Bilous et al. (2016),[10] we examined the TOA and DM perturbations due to the frequency-dependence of the profiles. These four profiles are shown in Figure 5; the trailing components are clearer at lower frequencies than at higher frequencies, suggesting that the shape variations as a function of time, as seen in Michilli et al. (2018), are also a function of frequency, at least for some epochs.

Bilous et al. (2016) used their observations to determine a new spin period and DM for each of the pulsars in their census. The initial adjustment of these two parameters maximized the pulse signal-to-noise ratio. Afterward, an average template was generated and used to calculate more precise TOAs and perform a subsequent timing analysis to improve their period and DM estimate. They did not account for profile evolution—either intrinsic or from interstellar scattering—in their work, but noted it as a potential bias. The profiles used in this analysis are therefore phase-aligned according to their method.

We generated smooth template shapes for each of the four profiles. While pulsar components are often fit with von Mises functions (e.g., Osłowski et al. 2011; Hassall et al. 2012), the circular analog of a Gaussian function, the automated routine in the PYPULSE package (Lam 2017) to fit multiple such components (see a more thorough description of the procedure conditions in Lam et al. 2019) did not converge for the lower-frequency profiles, due to the shapes of the trailing components. We then used a simpler Savitzky–Golay filter (Savitzky & Golay 1964), implemented in SCIPY with a moving 11 point cubic polynomial, which produced residuals between the template and the data profile at the level of the rms noise of the off-pulse region; slight variations in the parameters did not affect the overall fit significantly. With our four smooth pulse shapes, we used PYPULSE to fit the highest-frequency (178 MHz) template to the other three templates in order to compute the arrival-time offsets due to frequency-dependent profile evolution; these were 229.0, 75.7, and 11.2 μs for the 120, 139, and 159 MHz profiles, respectively. We chose the highest-frequency template as a standard of comparison to

---

[10] Obtained via the European Pulsar Network, http://www.jb.man.ac.uk/research/pulsar/Resources/epn/.

minimize the impact of the trailing component shapes as an approximation for the intrinsic pulse shape compared to a pulse shape showing a light echo.

Using these timing perturbations, we then calculated the estimated DM perturbations. See the Appendix for more on DM estimation in the presence of an additional chromatic perturbation—in this case, delays due to the pulse shape changes as a function of frequency. Since the method of calculating DM between Bilous et al. (2016) and this analysis are different, we do not expect the absolute DM value to be the same (Lam et al. 2016b). However, using the two lowest or highest frequencies to calculate the DM alone yielded a difference between the two of 1.7×10^{-3} pc cm^{-3}, again of the same amplitude of the variations seen by Donner et al. (2019). This value is an order of magnitude larger than the DM difference they quote between scattered and unscattered profiles. In performing their DM analysis, Donner et al. (2019) accounted for frequency-dependent profile evolution with a frequency-resolved template, which should then mitigate any impact of this profile evolution on the measured DMs. As mentioned previously, because their template was generated from an observation on MJD 57161, we expect the DM at both bands to be equal by construction at that epoch, which is also noted by the authors, though the true absolute DM between the two at that time and over the course of the entire observing span may differ. Nevertheless, the changing profile shapes as a function of time as seen in Donner et al. (2019) and in Michilli et al. (2018) could cause biases in the TOAs and the subsequent DM determinations, especially when coupled with the changes in frequency. Note again that Donner et al. (2019) did state the amplitude of scattering in their data and the biases in their DM; we find that this amplitude does not affect their conclusion that frequency-dependent DM is observed.

3.3. Impact of Arrival-time Uncertainties

We examined the role of additional components to the TOA uncertainties due to pulse jitter on the DM estimates. Traditionally, until the last several years, many analyses considered the TOA uncertainty as arising only from template fitting (e.g., Demorest et al. 2013; Manchester et al. 2013; Desvignes et al. 2016), the process of fitting a smoothed template shape to the data profile. The assumption of matched filtering underlying this fitting is that the data is a shifted and scaled copy of the template shape. It has been long known that single pulses from pulsars vary stochastically (Craft 1970), implying that the data shape cannot be an exact copy of a template since the average of a finite number of single pulses will always be slightly different. In general, shape changes due to jitter include contributions both from phase and amplitude variations.

We used the jitter parameter f_J defined in Cordes & Downs (1985) for our analysis, defined as the ratio between the single-pulse rms jitter and the equivalent rms (i.e., for a Gaussian pulse, the standard deviation as compared to the full width at half maximum) of the template (Shannon et al. 2014; Lam et al. 2016a). Cordes & Shannon (2010) summarized a number of analyses in the literature, primarily for canonical pulsars, and suggest that $f_J \approx 1/3 - 1/2$. Shannon et al. (2014) found similar values for millisecond pulsars. Lam et al. (2016a, 2019) used a separate jitter parameter that is independent of the pulse shape, but found comparable statistics for millisecond pulsars. In many cases, especially for bright canonical pulsars in which

single pulses can be detected, jitter is the dominant component of the TOA uncertainty (Lam et al. 2016a).

Again using profiles of PSR J2219+4754 from Bilous et al. (2016), calculating the pulse width, and assuming a fiducial value of $f_J = 1/3$, we found the rms single-pulse jitter for PSR J2219+4754 to be 1.2 ms, ≈0.2% of pulse phase ($P = 0.5385$ s), consistent with some pulsars in Lam et al. (2016a, 2019), though below the average. (Note that millisecond pulsar studies as described above were performed at significantly higher frequencies, and the statistics for millisecond pulsars may be different from that of canonical pulsars.) Since the rms jitter scales as the number of pulses $N_p^{-1/2}$, we assumed the pulsar was observed for the median observing time each epoch, 115 minutes, using the LOFAR station most used in Donner et al. (2019), DE605. Given the number of pulses in that time, we find that the TOA uncertainty due to jitter is ≈10 μs. Using a larger value of the jitter parameter(s) will yield a larger uncertainty. In addition, changes in the integration time will vary the TOA uncertainty; the integration times for DE605 ranged from 2 to 146 minutes, which yield an equivalent rms jitter of 79 μs to 9 μs, respectively.

We estimated the value of the TOA uncertainties as follows. Donner et al. (2019) stated a median DM uncertainty of 3.7×10^{-5} pc cm^{-3}. Following the formalism of Lam et al. (2015) and Cordes et al. (2016) of assuming that the (frequency-independent) DM is measured at two spot frequencies and then the infinite-frequency TOA is estimated by removing the dispersive delay, one can calculate the DM difference between the true DM and the estimated DM as

$$\delta\mathrm{DM} = -\frac{\epsilon_{\nu_1} - \epsilon_{\nu_2}}{K(\nu_1^{-2} - \nu_2^{-2})}, \qquad (11)$$

where $K \approx 4.149 \times 10^9$ μs MHz^2 pc^{-1} cm^3 is the dispersion constant (Lorimer & Kramer 2012) and σ_{ϵ_ν} is the rms timing uncertainty for frequency ν. (See the Appendix for more on this derivation and its effect on TOA perturbation.) The rms DM uncertainty, $\sigma_{\delta\mathrm{DM}}$, is then $\langle (\delta\mathrm{DM})^2 \rangle^{1/2}$. Assuming that σ_{ϵ_ν} is the same for the two halves of the LOFAR band and that $\sigma_{\delta\mathrm{DM}} = 3.7 \times 10^{-5}$ pc cm^{-3}, we find that $\sigma_{\epsilon_\nu} \approx 2.3$ μs, a factor of four smaller than the jitter uncertainty described above.

If the total TOA uncertainty is then the square root of the quadrature sum of the previous TOA uncertainty of 2.3 μs and the rms jitter of 10 μs, we can solve for the corrected rms DM uncertainty and find that $\sigma_{\delta\mathrm{DM}} = 1.7 \times 10^{-4}$ pc cm^{-3}. This is the rms DM uncertainty determined over the whole frequency band. Next, we calculate new DM uncertainties, assuming that DM is derived from each half of the band separately. We make sure to correct the TOA uncertainties for the change in the signal-to-noise ratio by a factor of $\sqrt{2}$, but assume no change in the jitter, as it is roughly frequency-independent over a small frequency range (Lam et al. 2019). This is in accordance with the procedure of Donner et al. (2019) to find the DM using measurements taken above and below 149 MHz. We split the full band into four and then used the centers of the bottom two frequency channels as our spot frequencies to determine the DM for data taken below 149 MHz. Correspondingly, the centers of the top two frequency channels were used to determine the DM for data taken above 149 MHz. We found that $\sigma_{\delta\mathrm{DM}} = (3–5) \times 10^{-4}$ pc cm^{-3}. This range of values is of an order similar to those of $\sigma_{\mathrm{DM}(\nu)}$ discussed in Section 2. Our

analysis describing the underestimation of the TOA uncertainties further strengthens the argument that differences in DM between the two frequency bands discussed in Donner et al. (2019) are less significant than were shown. We do note, however, that while the amplitude of these uncertainties adds significantly to the two DM time series, this is a white-noise contribution in time. Therefore, it cannot explain the systematic offsets between the two that are seen by Donner et al. (2019), i.e., frequency-dependent DM causes non-white-noise shifts in the TOAs, and so increasing the error bars does not remove the effect.

We also estimated the contribution to the TOA uncertainty from scintillation noise, also known as the "finite-scintle effect" (Cordes et al. 1990), one of three commonly analyzed white-noise contributions to the TOA uncertainty on short timescales (Lam et al. 2016a, 2018b). The scintillation timescale Δt_d can be found when the structure function of the electromagnetic phase perturbation is equal to unity, or alternatively in terms of the DM structure function (Lam et al. 2016b),

$$D_{\mathrm{DM}}(\Delta t_d) = 1.47 \times 10^{-15} \ (\mathrm{pc \ cm}^{-3})^2 \left(\frac{\nu}{\mathrm{GHz}}\right)^2. \quad (12)$$

Given that they observe $D_{\mathrm{DM}}(\tau) = 3.1 \times 10^{-10}$ (pc cm^{-3})^2 $(\tau/\mathrm{day})^{5/3}$, we found that $\Delta t_d = 5.7$ s. Due to the time-variability of the trailing components in the profile, we estimated the scattering timescale simply from NE2001 as $\tau_d = 0.4$ ms at 150 MHz, or an equivalent scintillation bandwidth of $\Delta \nu_d = 0.46$ kHz. The TOA uncertainty from scintillation noise is $\approx \tau_d / \sqrt{n_{\mathrm{ISS}}}$, where n_{ISS} is the number of scintles ("patches" of increased intensity in the time-frequency plane), given by

$$n_{\mathrm{ISS}} \approx \left(1 + \eta_t \frac{T}{\Delta t_d}\right)\left(1 + \eta_\nu \frac{B}{\Delta \nu_d}\right). \quad (13)$$

The filling factors η_t, η_ν are in the range 0.1–0.3, depending on the properties of the medium, and we have adopted a value of 0.2 for both (Cordes & Shannon 2010). Given an observation time $T = 115$ minutes and a bandwidth $B = 71.5$ MHz, we found that contribution of scintillation noise to the TOA uncertainty is 0.4 μs, much smaller than either the template-fitting component or the jitter component, and therefore it should not factor substantially into the error budget.

Finally, we looked at the impact of polarization calibration errors on the data (Stinebring et al. 1984). Foster et al. (2015) have shown that polarization leakage can result in significant TOA uncertainties ($\sim$microseconds) for well-timed millisecond pulsars. Gentile et al. (2018) showed that the stability of the Arecibo Observatory system varies quite dramatically between frequencies and epochs, and therefore recalibration must be performed per epoch. Given the errors, we performed an uncertainty analysis expanding upon the calibration procedure of Donner et al. (2019), who followed Noutsos et al. (2015), where PSR J2219+4754 itself was used to test the calibration stability of the LOFAR antennas. Noutsos et al. (2015) stated that systematic uncertainties in the polarization leakage are on the order of 5–10%.

Donner et al. (2019) performed observations at or close to transit, and therefore claim that imperfections in the calibration did not affect the analysis. However, Noutsos et al. (2015) showed that at hour angles far away from transit, the profile

differences for PSR J2219+4754 can be as large as 30% compared with at transit for the circularly polarized flux. While the observations Donner et al. (2019) performed were closer to transit, we would still expect pulse shape deviations on the order of a few percent, given the observation lengths alone.

Following Cordes et al. (2004), the TOA uncertainty due to pulse shape changes from an incorrect absolute gain calibration is

$$\sigma_{\mathrm{pol}} \sim 1 \ \mu\mathrm{s} \ \left(\frac{\varepsilon}{0.1}\right)\left(\frac{\pi_{\mathrm{V}}}{0.1}\right)\left(\frac{W}{100 \ \mu\mathrm{s}}\right), \quad (14)$$

where we provide fiducial values as in Lam et al. (2016a, 2018b) for the fractional gain error ε, degree of circular polarization π_{V}, and pulse width W. Using Equation (15) as a crude estimator, with a pulse with of $\sim$8 ms, a circular polarization fraction of 9% (Noutsos et al. 2015), and assuming $\varepsilon \sim 0.1$ (the gain error and polarization leakage are not entirely equivalent quantities, but we take the fractional errors above as representative), then the component of the TOA uncertainty is $\sim$72 μs, many times larger than the template-fitting errors. If polarization error yields a consistent offset/perturbation in the arrival times, then the net stochastic TOA uncertainty is zero and the frequency-dependent DM analysis should not be affected. However, given analyses such as that of Gentile et al. (2018) regarding system stability, we do not expect these calibration errors to be systematic alone. While PSR J2219+4754 is not a millisecond pulsar, we see that it is quite likely that polarization calibration errors on the order of microseconds or tens of microseconds are expected (see again Foster et al. 2015). Because these are comparable to the template-fitting errors, they should further be accounted for in dispersive-delay removal.

3.4. Impact of a DM Gradient or Scattering Screen on the Structure Functions

Any additional structure in the DM time series beyond that from a turbulent medium will increase the measured structure function (Lam et al. 2016b; Jones et al. 2017). For the following analysis, we will make a distinction between the first-order structure function $D_{\mathrm{DM}}^{(1)}(\tau)$ that we have implicitly discussed previously and the second-order structure function $D_{\mathrm{DM}}^{(2)}(\tau)$, both defined as follows:

$$\begin{aligned} D_{\mathrm{DM}}^{(1)}(\tau) &\equiv \langle [\mathrm{DM}(t + \tau) - \mathrm{DM}(t)]^2 \rangle, \\ D_{\mathrm{DM}}^{(2)}(\tau) &\equiv \langle [\mathrm{DM}(t + \tau) - 2\mathrm{DM}(t) + \mathrm{DM}(t - \tau)]^2 \rangle. \end{aligned} \quad (15)$$

While the first-order structure function will remove any constant term from the time series (e.g., the mean), the second-order structure function removes linear terms and can be used to detect discrete changes in any underlying linear trends in the DM time series (Lam et al. 2016b). The latter can also be thought of as related to the curvature of the time series. For a Kolmogorov medium, it is proportional to the first-order structure function (Lam et al. 2016b, Appendix A). Again, any additional structures beyond a turbulent medium seen in the time series will increase these measured quantities.

To understand the impact of a DM gradient or ESE on the structure functions of both orders, we performed simulations (as in Lam et al. 2015, 2016b) of red-noise realizations of DM
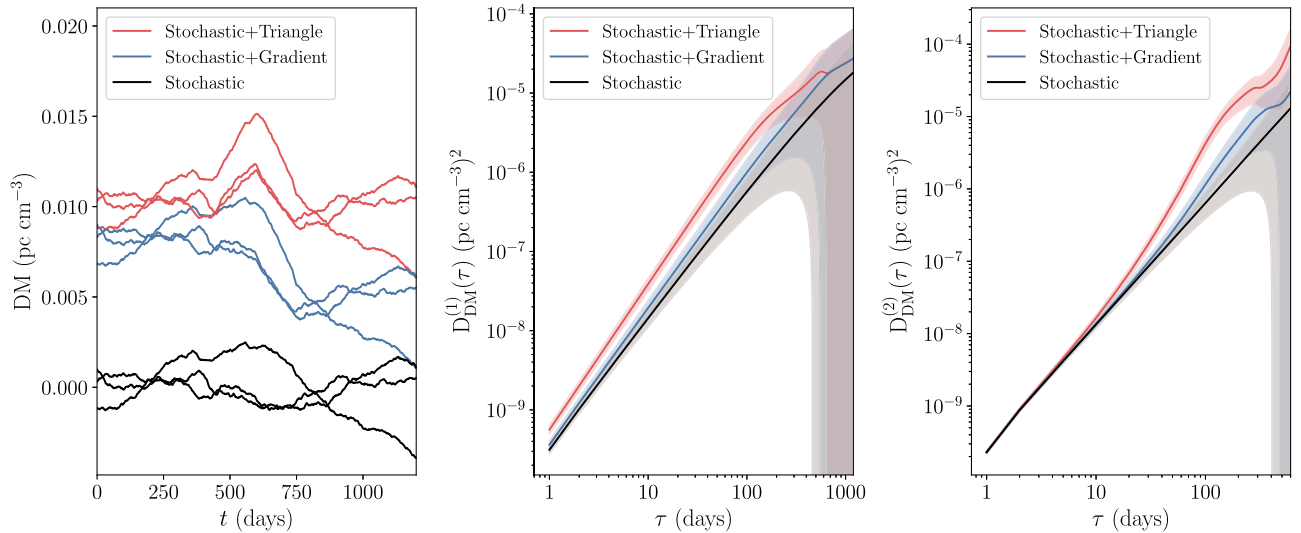
Figure 6. DM time series (left) along with their associated first- (middle) and second-order (right) structure functions. We plot the first three (arbitrary) time series (in order from bottom to top) we generated of the stochastic DM component (black) and added in a gradient (blue) or a triangle function representing an ESE (red). We offset the time series by $+0.005$ pc cm^{-3} between each set of three for visual clarity. The corresponding structure functions have the same colors, where the lines and the shaded regions represent the mean and standard deviation, respectively. See text for more information.

time series. We generated 10,000 realizations of 1200 day DM time series from a stochastic Kolmogorov medium for which the amplitude was set by the measured structure function $D_{DM}^{(1)}(\tau) = 3.1 \times 10^{-10}$ (pc cm^{-3})$^2 (\tau/\text{day})^{5/3}$. Next, we added a gradient with slope 2×10^{-5} pc cm^{-3} day^{-1} and of length 150 days into each time series. To avoid a discontinuity, we added a baseline value of 3×10^{-3} pc cm^{-3} to the higher side of the gradient (i.e., in total, we added a slanted step function). Last, we added a triangle function representing an ESE into each stochastic realization (separate from the gradient), with slope 2×10^{-3} pc cm^{-3} day^{-1} and of length 150 days on either side. Figure 6 (left panel) shows several of these time series.

As expected, we see in the first-order structure functions shown in the middle panel that there is an increase in the amplitude as well as a changing slope, though the mean stochastic + gradient structure function is within one standard deviation of the mean stochastic-only structure function. Note that because the length of the actual time series is only 1200 days, the range of $D_{DM}^{(1)}$ at large lag varies significantly from the mean at lags greater than a few hundred days.[11] Since only a few increments (DM differences) contribute to the averages in the bins at large lags, we do expect a wide variation as we see in Figure 6 and in previous simulations of ours (Lam et al. 2015, 2016b).

If either a density gradient or an ESE is along the line of sight, then the stochastic Kolmogorov component of the measured first-order structure function should be lower in amplitude than previously reported, thereby lowering the measured SM or raising the scintillation timescale. While the slope of the mean first-order structure function for the stochastic + triangle simulations has a steeper slope, the "realization errors" on the structure function for the stochastic-only simulations can lead to both steeper or shallower slopes for a single measured structure function, which must be accounted for when performing these

analyses to constrain the consistency of the spectrum with a Kolmogorov medium without bias (Lam et al. 2016b; Jones et al. 2017).

Analyses of the second-order DM structure function have not been performed in the literature. We show the results of the analysis of our simulations in the right panel of Figure 6. We notice two features. First, all three structure functions tend toward the same value at low time lags, which may then allow for a more robust estimate of the scintillation timescale (or alternatively, the SM as in Donner et al. 2019) as per Appendix A of Lam et al. (2016b), and therefore the amplitude of the frequency-dependent DM. Second, we see that adding extra components to the DM time series on top of the purely stochastic term will produce a more pronounced increase in the value of the second-order structure function at a time lag of ~150 days, the timescale of the injected structures. There is still some slight overlap in the mean stochastic + gradient versus the mean stochastic-only second-order structure function.

To test our simulations, we used the values of the two DM time series estimated for different frequencies as provided in Donner et al. (2019) to calculate both the first- and second-order structure functions for each, shown in Figure 7. The gray regions are the same as in Figure 6 for the stochastic-only simulations, again scaled to the amplitude they estimate of $D_{DM}^{(1)}(\tau) = 3.1 \times 10^{-10}$ (pc cm^{-3})$^2 (\tau/\text{day})^{5/3}$. Recall that no white noise has been added to our simulations, and therefore there is no flattening of the simulated structure functions as compared with the values estimated from the data. We see significant spread in the values of both structure functions at low lags, due partially to the white noise and partially to the irregular sampling at small lags.

For the first-order structure function, we see no increase in the values for $\tau \gtrsim 100$ days indicative of a discrete structure or gradient as analyzed in our simulations (see again Figure 6). Additionally, we see that the gray regions for the second-order structure function do not well-represent the data for most lags, and we also do not see the equivalent increase at large lags if a discrete structure was present.

---

[11] Note that Donner et al. (2019) calculate the standard deviation of the base-10 logarithm of the structure function, whereas here we calculate the standard deviation of the structure function itself.
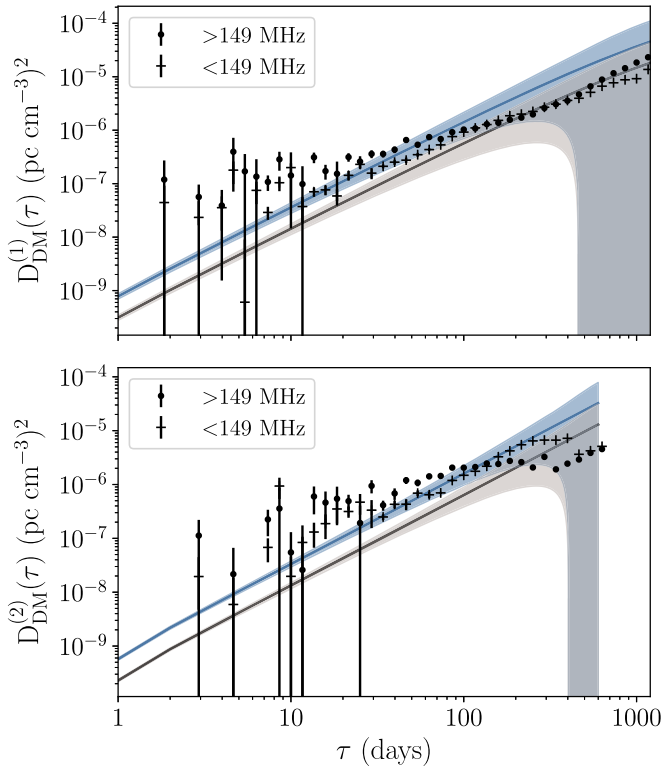
Figure 7. First- (top) and second-order (bottom) structure functions for the two DM time series estimated for different frequencies (the symbols representing the two frequency ranges) as shown in Donner et al. (2019). Gray region denotes the simulations as shown in Figure 6 for the stochastic-only medium with the amplitude set by that estimated in Donner et al. (2019). Blue region denotes those scaled by a factor of 2.5, showing greater consistency with both structure functions.

By increasing the overall amplitude of the simulated structure functions, we see greater agreement with the data, which can be used to extract information about the medium. Because fitting of the structure functions—or even the increments—can be complex, as noted previously (Lam et al. 2016b; Jones et al. 2017), we decided instead to visually increase the values only for demonstrative purposes about the utility of these estimates. We increased the simulated structure functions by a factor of 2.5, as seen in the blue shaded regions in Figure 7. The greater consistency with the data points is easily visible. Since $\sigma_{\mathrm{DM}(\nu)} \propto \mathrm{SM} \propto C_n^2 \propto D_{\mathrm{DM}}^{(1)}$ (see Equation (2), and also Cordes et al. 2016; Lam et al. 2016b), then a factor of 2.5 increase in the structure function translates to the same increase in $\sigma_{\mathrm{DM}(\nu)}$.

However, the observed rms difference we calculated between the two DM time series was 0.7×10^{-3} pc cm^{-3} (see also Figure 6 of Donner et al. 2019), which was in agreement with the prediction for a uniform Kolmogorov medium discussed in Section 2. Since the rms difference[12] in the frequency-dependent DM is increasing by a factor of 2.5 due to an increase in the estimated $D_{\mathrm{DM}}^{(1)}$, or alternatively the SM, then we find disagreement with the initial assumption of the line of sight being a uniform Kolmogorov medium.

One common model for describing the ISM along the line of sight is not as uniform, but instead uses a thin scattering screen

---

[12] Note that, while the structure function typically is proportional to the variance of a time series at a given lag, in this case we are looking at the proportionality with the rms frequency-dependent DM rather than the rms of the DM time series.

model because the mathematics are simpler and the resulting quantities in a calculation depend only on geometric terms (Cordes et al. 1986; Cordes & Rickett 1998). The geometry of the screen is independent from the spectral index (i.e., Kolmogorov or otherwise). Such a model can also physically describe regions of larger-scale overdense structure in the ISM. Rather than assuming that the medium along the line of sight is entirely uniform, we can quantify what effect a factor of 2.5 increase in the structure function implies if we assume the thin-screen model. In Equation (2), we provided the geometric factor $G_{11/3} = 0.145$ for a uniform medium via Cordes et al. (2016). If instead we assume a screen at distance D_s from the pulsar, at distance D, then the geometric factor becomes $G_{11/3} = [x(1-x)]^{5/6}$, where $x = D_s/D$ is the screen's fractional distance between the pulsar and us. Note that the function is symmetric about the halfway ($x = 0.5$) point. Assuming a screen describes the line of sight allows us to simultaneously increase the SM while decreasing the value of $G_{11/3}$ to keep $\sigma_{\mathrm{DM}(\nu)}$ fixed at its observed value. Taking the observed DM difference rms and using Equation (2) to instead determine $G_{11/3}$ and therefore x, we found that $x = 0.045$ or $x = 0.955$, i.e., the screen is at a distance 0.1 kpc from either the pulsar or the Earth. In the case of the latter, this nominal distance lies a factor of a few beyond that of the Local Bubble (Frisch et al. 2011). An $x \approx 0.98$ would place the screen in the rough appropriate location (~ 40 pc), which in turn decreases $G_{11/3}$ or increases the structure functions by an additional factor of 2, which starts to come in tension with the values shown in Figure 7. However, since the pulsar's distance is uncertain due to estimation with the NE2001 model, the Local Bubble could still be a plausible location of a screen.

Since $G_{11/3}$ and therefore $\sigma_{\mathrm{DM}(\nu)}$ increases as x tends toward the midpoint of the line of sight, we can rule out any screen structure much closer than the endpoints of the line of sight since the estimated structure functions would be in greater tension with those observed. Our method demonstrates that we can simultaneously use the variations in the DM time series taken at different frequencies along with the variations of the differences between the two DM time series to constrain the location of an assumed screen quite strongly. Future observations of this and other pulsars taken at widely separated frequencies with high cadence may be able to jointly model even higher-order structure functions for even further constraining power.

Due to the irregular sampling in DM time series that is common for many pulsar observations, it may be preferred to analyze the individual second-order increments ($\mathrm{DM}(t+\tau) - 2\mathrm{DM}(t) + \mathrm{DM}(t-\tau)$, which are squared and averaged over to obtain $D_{\mathrm{DM}}^{(2)}$) as was done for PSR B1534+12 in Lam et al. (2016b), rather than the second-order structure function as performed here. However, the high-cadence of observations in Donner et al. (2019), combined with the duration, have allowed us to directly calculate the second-order structure function rather than simply the increments. Continued observations, especially with a dense high-cadence program, could help constrain the values of both structure functions at smaller lags.

Note that the large transverse velocity means that the motion of the pulsar across the sky is fairly straight (e.g., the parallax motion is small; see trajectory plots in Jones et al. 2017). The quasi-periodic variations in the DM time series that deviate from a purely power-law spectrum, as seen in Madison et al. (2019) due to the line-of-sight crossing correlated spatial DM

fluctuations, should therefore be small and not impact the power spectrum/structure function significantly. Put another way, while the assumption of the line-of-sight crossing independent DM fluctuations is broken and we expect short-term rapid variations in the DM that might impact the measured structure function, we expect this change to be negligible for this pulsar.

In conclusion, the consistency of the structure functions with a Kolmogorov model over the range of time and spatial scales observed suggests that the medium is turbulent down to 10 s of days or ~1 au (for an assumed lens at distance 1.1 kpc). As discussed, below this scale the structure function appears dominated by white-noise fluctuations given the cadence of observations, which causes the observed structure function/spectrum to become shallower. The $L = 20$ au lens size (equivalent to the 300 day timescale) should be seen as a steepening in the structure function as shown in Figure 6. In addition, any truly stochastic process with a spectrum steeper than that of a Kolmogorov medium, which could then produce strong refractive effects (Cordes et al. 1986), is also unseen in the structure functions in Figure 7.

4. Impact on Precision Timing

Temporal and frequency-dependent DM variations will have significant impacts on high-precision pulsar timing experiments, including the efforts to detect low-frequency gravitational waves. While these topics have been discussed in the literature (see, e.g., You et al. 2007a; Keith et al. 2013; Lee et al. 2014; Cordes et al. 2016; Lam et al. 2016b), we will take the analysis of Donner et al. (2019) further and discuss the impact in the context of our accounting of the various noise processes in the real data.

Donner et al. (2019) estimated the limiting TOA precision by considering observations at 1.4 GHz with a relatively limited 250 MHz bandwidth (20% bandwidth). However, current pulsar backend systems can process up to 800 MHz of bandwidth (see, e.g., the Appendix of Dolch et al. 2014) and techniques have been developed to process even larger bandwidths (e.g., Dunning et al. 2015) while simultaneously compensating for the DM (Pennucci et al. 2014). More generally, a common practice is to conduct simultaneous or near-simultaneous observations at two frequencies. For example, the North American Nanohertz Observatory for Gravitational Waves (NANOGrav) uses combinations of 0.8 GHz and 1.4 GHz for some pulsars and 1.4–2.3 GHz for some others (Arzoumanian et al. 2018), from which even higher-precision DM estimates can be obtained.

When only purely dispersive delays factor into TOAs measured at two spot frequencies, the rms TOA is given by (see the Appendix. but also Lee et al. 2014, Equation (12); Lam et al. 2018b, Table 1),

$$\sigma_{\delta t_\infty} = \left(\frac{\sigma_{\epsilon_{\nu_1}}^2 + r^4 \sigma_{\epsilon_{\nu_2}}^2}{(r^2 - 1)^2} \right)^{1/2}, \qquad (16)$$

where again σ_{ϵ_ν} is the rms timing uncertainty for frequency ν. This timing uncertainty includes all sources of white noise that affect the TOA estimation, such as from radiometer noise or jitter (see, e.g., Lam et al. 2018b). A critical aspect of Equation (17) is that the rms TOA is dependent only on r and not a specific frequency. It does not matter whether the timing

measurements are acquired at low or high frequencies, so long as the individual frequency-channel TOA uncertainties are the same for a given value of r.

As an illustration, taking $r \sim 2$ and setting $\sigma_{\epsilon_\nu} = \sigma_{\epsilon_{\nu_1}} = \sigma_{\epsilon_{\nu_2}}$, then $\sigma_{\delta t_\infty} = 1.4 \sigma_{\epsilon_\nu}$. Therefore, in cases where the median TOA uncertainty from finite pulse signal-to-noise ratio is small (i.e., well below 1 μs), such as reported per-pulsar and per-band in the NANOGrav 11 yr Data Set (Arzoumanian et al. 2018), then the requirement for submicrosecond-precision timing is met. Several other sources of error, such as from pulse phase jitter, are known to be much smaller than this limit (Lam et al. 2019). Therefore, using low-frequency timing data to increase r will quantitatively improve the timing of many pulsars, as long as the TOA uncertainties for pulses at those frequencies are low enough and unmitigated ISM effects are small, e.g., typically for pulsars with lower DM values (Lam et al. 2018b).

As an extreme case, we considered $\sigma_{\epsilon_{\nu_2}} \to 0$. In this case, the overall timing precision will be dominated by the precision at the lower frequency, $\sigma_{\delta t_\infty} \approx \sigma_{\epsilon_{\nu_1}}/(r^2 - 1)$. For a sufficiently large value of r, the timing precision due to DM uncertainty or variations could be made negligible. As a specific example, with relevance to the data presented by Donner et al. (2019), we considered $r \approx 10$, equivalent to $\nu_1 \approx 140$ MHz and $\nu_2 \approx 1400$ MHz. In this hypothetical example, a timing precision $\sigma_{\delta t_\infty} \approx 10$ ns could be obtained, if $\sigma_{\epsilon_{\nu_1}} \approx 1$ μs. We chose this illustration because a timing precision of order 10 ns is comparable to the expected precision required for the study of gravitational waves.

Of course, this timing improvement neglects the uncertainties due to frequency-dependent DM as discussed by Cordes et al. (2016). The amplitude of the differences in DM between frequencies also depends on r (as well as the specific frequency choices), but the net effect on the overall timing precision can be quantified and then built into noise models, e.g., via covariance matrices such as constructed in Lam et al. (2018b). Cordes et al. (2016, see Figures 7 and 8) show that, for pulsars with DM $\lesssim 30$ pc cm^{-3}, combining data from the 100 MHz and 2 GHz regimes will yield TOA errors that still meet the requirement of sub-microsecond precision, especially as current and future telescopes come online, drastically reducing the template-fitting errors from finite pulse signal-to-noise ratio. Many pulsars used in precision-timing experiments have DM values in this range (Verbiest et al. 2016). Cordes et al. (2016) also discussed fitting a wide range of frequencies versus only two spot values. As expected, the increase in frequency coverage can, in many cases, improve the timing precision over the case where only two spot frequencies are used—which is no longer the case for many modern precision-pulsar-timing experiments (Verbiest et al. 2016).

Unmitigated chromatic delays will also add to the TOA uncertainties (Lam et al. 2018b, Table 1) and cause frequency-dependent excess noise in the timing residuals (Lentati et al. 2016; Lam et al. 2017). However, even for the pulsar with the highest DM millisecond pulsar used in precision timing, PSR J1903+0327 (DM ≈ 300 pc cm^{-3}), observed between roughly 1.1 and 2.5 GHz, the long-term rms residual is 4 μs, though a significant portion of that rms is again from frequency-dependent excess noise (Lam et al. 2017), which future timing methodologies might be able to partially mitigate (Shannon & Cordes 2017).

Last, we expand on the discussion in Donner et al. (2019) that, at higher frequencies, longer-term DM variations are of

particular importance to take into account for timing data. Given that the frequency-dependent DM comes from differences in ray-path averaging, whereas the trends in DM come from the relative Earth-pulsar motion along the line of sight, we expect the longer-term DM variations to track each other between frequencies, regardless of frequency; Donner et al. (2019) also agree with this given their analysis. However, in terms of the overall timing, it is the lower frequencies that are impacted much more heavily since the dispersive delays are weighted by ν^{-2}. At frequencies much higher than typically used in precision timing, the dispersive delay becomes small and thus any changes in the dispersive delay are also small; as an extreme, X-ray pulsar data do not require DM corrections of any kind.

As an additional consideration, it is important to remember that short-term DM variations that are improperly corrected for can contribute heavily to the overall rms timing, and may not contribute as simple white noise (e.g., Lam et al. 2015). Many pulsars in precision-timing experiments show very rapid timescales for DM to vary (Jones et al. 2017), including from the solar wind (You et al. 2007b; Madison et al. 2019; see also Howard et al. 2016 for the study of a coronal mass ejection with a slow-period pulsar) or structures in the ISM (e.g., Fonseca et al. 2014; Coles et al. 2015; Lam et al. 2018a).

5. Discussion

In this work, we have described the requirements necessary for observational tests separating the effects of frequency-dependent DM from refractive lensing. The observations shown in Donner et al. (2019) provide an excellent test of frequency-dependent DM as laid out by Cordes et al. (2016). While the theoretical treatment considers the ability to perfectly measure DM at a given spot frequency, going forward, analyses of observations of the kind reported in Donner et al. (2019) must account for the wide range of different TOA uncertainty components and ISM propagation effects presented in this work. We showed here that, even for a canonical pulsar versus a millisecond pulsar, the recent work done in precision-timing experiments has become relevant, given the timing quality of the pulsars and the instrumentation used to access to new types of observations, e.g., low-frequency observations via LOFAR as described here. Furthermore, while canonical pulsars may not provide constraints on the same tests of fundamental physics as millisecond pulsars, their use in studying variations in the ionized ISM along many different lines of sight (e.g., Petroff et al. 2013) will be unparalleled, given the greater population of them over millisecond pulsars, especially if observations covering a large frequency ratio can be leveraged.

While we have focused our analyses on the plasma lens as described by Donner et al. (2019), we have not discussed the potential causes of the light echoes as seen by Michilli et al. (2018). They described the similarities between their pulse profiles and those seen in PSR B0531+21 (the Crab Pulsar), though those profile variations are attributed to structure in the local environment in the nebula surrounding the pulsar (Backer et al. 2000; Lyne et al. 2001). While an interstellar lens would produce a negligible effect if very close to the pulsar, as shown in Figure 3, the model proposed by Backer et al. (2000) involves the pulsar traversing near material (a prism geometry) close enough that emission at different frequencies passes through different electron content at different times (a true

dispersive delay, whereas they argue that the refractive geometric delay will be significantly smaller) while that of Lyne et al. (2001) involves reflections of the images. Note that the fact that the Crab Pulsar has both a main pulse and interpulse means that propagation variations will affect both in the same way, making it easier to disentangle from intrinsic profile shape variations. Both of the proposed mechanisms could be examined in more detail with respect to the pulse profiles shown in Michilli et al. (2018). In a combined analysis, if the variability is also tied to the DM variations shown in Donner et al. (2019), then the total data set will provide an excellent probe of the material local to PSR J2219+4754, though such variations will then need to be disentangled from the variability expected from a turbulent medium with which we have shown consistency.

Identifying ESEs or other "ISM events" seen in pulsar timing data in near-real time will allow for more intensive follow-up observations, including a higher cadence of observations over many frequencies and using different observatories worldwide, especially if dynamic spectra with resolved scintles can be obtained (Hewish 1980; Stinebring et al. 2001). The characteristic timescale and bandwidth can be used to constrain the location of a lensing structure (Cordes & Rickett 1998), while the drift rate ("rotation") of the scintles provides the component of the refractive angle in the direction of the pulsar's motion (Hewish et al. 1985; Cordes et al. 1986), providing partial information on the geometric time delay. Interferometric observations can help constrain the changing position and sizes of the pulsar image (Blandford & Narayan 1985), or possibly multiple images (Cordes & Wolszczan 1986; Cordes et al. 2017), providing additional constraints on the lensing geometry over the line of sight. Any such additional observations will allow us to resolve small-scale structure in the ISM and probe the Galactic population of these lenses.

Appendix
DM Estimation with Additional Chromatic Errors

As a useful reference, here we will describe DM estimation from observations taken at two spot frequencies with additional chromatic errors following the formalism of Lam et al. (2015) and Cordes et al. (2016). We can write the TOA at a particular frequency ν as the infinite-frequency arrival time plus the dispersive delay term. For this calculation, we will also include measurement errors ϵ_ν and a chromatic (frequency-dependent) timing perturbation $t_{C,\nu}$, such that

$$t_\nu = t_\infty + \frac{K\mathrm{DM}}{\nu^2} + t_{C,\nu} + \epsilon_\nu. \tag{17}$$

Here, $K \approx 4.149 \times 10^9 \ \mu\mathrm{s} \ \mathrm{MHz}^2 \ \mathrm{pc}^{-1} \ \mathrm{cm}^3$ is the dispersion constant in observationally convenient units (Lorimer & Kramer 2012). We estimate the DM by taking TOAs at two

frequencies ν_1 and ν_2 and calculating

$$\widehat{\mathrm{DM}} = \frac{t_{\nu_1} - t_{\nu_2}}{K(\nu_1^{-2} - \nu_2^{-2})}. \tag{18}$$

As in the main text, we will define the frequency ratio $r \equiv \nu_2/\nu_1$ with $\nu_1 < \nu_2$. The estimated infinite-frequency arrival time can then be written in one of two ways as

$$\hat{t}_\infty = t_{\nu_1} - \frac{K\widehat{\mathrm{DM}}}{\nu_1^2} = t_\infty + \frac{K(\mathrm{DM} - \widehat{\mathrm{DM}})}{\nu_1^2} + t_{C,\nu_1} + \epsilon_{\nu_1}$$

$$= t_{\nu_2} - \frac{K\widehat{\mathrm{DM}}}{\nu_2^2} = t_\infty + \frac{K(\mathrm{DM} - \widehat{\mathrm{DM}})}{\nu_2^2} + t_{C,\nu_2} + \epsilon_{\nu_2}. \tag{19}$$

We will now solve for the DM difference. Substituting the measured TOAs t_ν into the equation for $\widehat{\mathrm{DM}}$ and subtracting from the true DM, we have

$$\delta\mathrm{DM} \equiv \mathrm{DM} - \widehat{\mathrm{DM}} = \mathrm{DM} - \frac{t_{\nu_1} - t_{\nu_2}}{K(\nu_1^{-2} - \nu_2^{-2})}$$

$$= -\frac{t_{C,\nu_1} - t_{C,\nu_2} + \epsilon_{\nu_1} - \epsilon_{\nu_2}}{K(\nu_1^{-2} - \nu_2^{-2})}. \tag{20}$$

The TOA perturbation will be

$$\delta t_\infty \equiv t_\infty - \hat{t}_\infty = -\frac{K(\mathrm{DM} - \widehat{\mathrm{DM}})}{\nu_2^2} - t_{C,\nu_2} - \epsilon_{\nu_2}$$

$$= \frac{-r^2 t_{C,\nu_2} - r^2\epsilon_{\nu_2} + t_{C,\nu_1} + \epsilon_{\nu_1}}{r^2 - 1}. \tag{21}$$

When the chromatic offsets are zero, we arrive at simply

$$\delta t_\infty = \frac{\epsilon_{\nu_1} - r^2\epsilon_{\nu_2}}{r^2 - 1}, \tag{22}$$

which agrees with Equation (21) in Cordes et al. (2016), assuming the frequency-dependent DM term is zero.

Equation (22) provides the timing offset but one must consider the TOA uncertainty, $\sigma_{\delta t_\infty}$, from the variance

$$\sigma_{\delta t_\infty}^2 = \langle \delta t_\infty^2 \rangle = \left\langle \left(\frac{\epsilon_{\nu_1} - r^2\epsilon_{\nu_2}}{r^2 - 1} \right)^2 \right\rangle. \tag{23}$$

We have assumed here that $\langle \delta t_\infty \rangle = 0$, which will be true if the errors ϵ_ν are Gaussian-distributed. If they are, and with variance $\sigma_{\epsilon_\nu}^2$, then the sum of the two terms in the numerator of Equation (23) will be Gaussian-distributed, which when squared will then be χ^2-distributed. Taking the expected value of the resultant quantity yields

$$\sigma_{\delta t_\infty}^2 = \frac{\sigma_{\epsilon_{\nu_1}}^2 + r^4\sigma_{\epsilon_{\nu_2}}^2}{(r^2 - 1)^2}. \tag{24}$$

If the TOA uncertainties are the same at both frequencies, such that $\sigma_{\epsilon_{\nu_1}} = \sigma_{\epsilon_{\nu_2}} = \sigma_{\epsilon_\nu}$, then we have

$$\sigma_{\delta t_\infty} = \sqrt{\langle \delta t_\infty^2 \rangle} = \sigma_{\epsilon_\nu}\left(\frac{r^4 + 1}{r^4 - 2r^2 + 1} \right)^{1/2}. \tag{25}$$

ORCID iDs

M. T. Lam https://orcid.org/0000-0003-0721-651X
T. Dolch https://orcid.org/0000-0001-8885-6388
M. L. Jones https://orcid.org/0000-0001-6607-3710
M. A. McLaughlin https://orcid.org/0000-0001-7697-7422
D. R. Stinebring https://orcid.org/0000-0002-1797-3277
M. Surnis https://orcid.org/0000-0002-9507-6985

References

Armstrong, J. W., Rickett, B. J., & Spangler, S. R. 1995, ApJ, 443, 209
Arzoumanian, Z., Brazier, A., Burke-Spolaor, S., et al. 2018, ApJS, 235, 37
Backer, D. C., Hama, S., van Hook, S., & Foster, R. S. 1993, ApJ, 404, 636
Backer, D. C., Wong, T., & Valanju, J. 2000, ApJ, 543, 740
Bilous, A. V., Kondratiev, V. I., Kramer, M., et al. 2016, A&A, 591, A134
Blandford, R., & Narayan, R. 1985, MNRAS, 213, 591
Clegg, A. W., Fey, A. L., & Lazio, T. J. W. 1998, ApJ, 496, 253
Cognard, I., Bourgois, G., Lestrade, J.-F., et al. 1993, Natur, 366, 320
Coles, W. A., Kerr, M., Shannon, R. M., et al. 2015, ApJ, 808, 113
Cordes, J. M., & Downs, G. S. 1985, ApJS, 59, 343
Cordes, J. M., Kramer, M., Lazio, T. J. W., et al. 2004, NewAR, 48, 1413
Cordes, J. M., & Lazio, T. J. W. 2002, arXiv:astro-ph/0207156
Cordes, J. M., Pidwerbetsky, A., & Lovelace, R. V. E. 1986, ApJ, 310, 737
Cordes, J. M., & Rickett, B. J. 1998, ApJ, 507, 846
Cordes, J. M., & Shannon, R. M. 2010, arXiv:1010.3785
Cordes, J. M., Shannon, R. M., & Stinebring, D. R. 2016, ApJ, 817, 16
Cordes, J. M., Wasserman, I., Hessels, J. W. T., et al. 2017, ApJ, 842, 35
Cordes, J. M., & Wolszczan, A. 1986, ApJL, 307, L27
Cordes, J. M., Wolszczan, A., Dewey, R. J., Blaskiewicz, M., & Stinebring, D. R. 1990, ApJ, 349, 245
Craft, H. D., Jr. 1970, PhD thesis, Cornell Univ.
Demorest, P. B. 2007, PhD thesis, Univ. California, Berkeley
Demorest, P. B., Ferdman, R. D., Gonzalez, M. E., et al. 2013, ApJ, 762, 94
Desvignes, G., Caballero, R. N., Lentati, L., et al. 2016, MNRAS, 458, 3341
Dolch, T., Lam, M. T., Cordes, J., et al. 2014, ApJ, 794, 21
Donner, J. Y., Verbiest, J. P. W., Tiburzi, C., et al. 2019, A&A, 624, A22
Dunning, A., Bowen, M., Bourne, M., Hayman, D., & Smith, S. L. 2015, in 2015 IEEE-APS Topical Conf. Antennas and Propagation in Wireless Communications (APWC) (Piscataway, NJ: IEEE), 787
Fiedler, R., Pauls, T., Johnston, K. J., & Dennison, B. 1994, ApJ, 430, 595
Fiedler, R. L., Dennison, B., Johnston, K. J., & Hewish, A. 1987, Natur, 326, 675
Fonseca, E., Stairs, I. H., & Thorsett, S. E. 2014, ApJ, 787, 82
Foster, G., Karastergiou, A., Paulin, R., et al. 2015, MNRAS, 453, 1489
Foster, R. S., & Cordes, J. M. 1990, ApJ, 364, 123
Frisch, P. C., Redfield, S., & Slavin, J. D. 2011, ARA&A, 49, 237
Gentile, P. A., McLaughlin, M. A., Demorest, P. B., et al. 2018, ApJ, 862, 47
Hassall, T. E., Stappers, B. W., Hessels, J. W. T., et al. 2012, A&A, 543, A66
Hewish, A. 1980, MNRAS, 192, 799
Hewish, A., Wolszczan, A., & Graham, D. A. 1985, MNRAS, 213, 167
Hobbs, G., Lyne, A. G., Kramer, M., Martin, C. E., & Jordan, C. 2004, MNRAS, 353, 1311
Howard, T. A., Stovall, K., Dowell, J., Taylor, G. B., & White, S. M. 2016, ApJ, 831, 208
Jones, M. L., McLaughlin, M. A., Lam, M. T., et al. 2017, ApJ, 841, 125
Keith, M. J., Coles, W., Shannon, R. M., et al. 2013, MNRAS, 429, 2161
Lam, M. T. 2017, PyPulse, Astrophysics Source Code Library, ascl:1706.011s
Lam, M. T., Cordes, J. M., Chatterjee, S., et al. 2016a, ApJ, 819, 155
Lam, M. T., Cordes, J. M., Chatterjee, S., et al. 2016b, ApJ, 821, 66
Lam, M. T., Cordes, J. M., Chatterjee, S., et al. 2017, ApJ, 834, 35
Lam, M. T., Cordes, J. M., Chatterjee, S., & Dolch, T. 2015, ApJ, 801, 130
Lam, M. T., Ellis, J. A., Grillo, G., et al. 2018a, ApJ, 861, 132
Lam, M. T., McLaughlin, M. A., Arzoumanian, Z., et al. 2019, ApJ, 872, 193
Lam, M. T., McLaughlin, M. A., Cordes, J. M., Chatterjee, S., & Lazio, T. J. W. 2018b, ApJ, 861, 12
Lee, K. J., Bassa, C. G., Janssen, G. H., et al. 2014, MNRAS, 441, 2831
Lentati, L., Shannon, R. M., Coles, W. A., et al. 2016, MNRAS, 458, 2161
Levin, L., McLaughlin, M. A., Jones, G., et al. 2016, ApJ, 818, 166
Lorimer, D. R., & Kramer, M. 2012, in Handbook of Pulsar Astronomy, ed. D. R. Lorimer & M. Kramer (Cambridge: Cambridge Univ. Press)
Lyne, A. G., Pritchard, R. S., & Graham-Smith, F. 2001, MNRAS, 321, 67
Madison, D. R., Cordes, J. M., Arzoumanian, Z., et al. 2019, ApJ, 872, 150

Maitia, V., Lestrade, J.-F., & Cognard, I. 2003, ApJ, 582, 972
Manchester, R. N., Hobbs, G., Bailes, M., et al. 2013, PASA, 30, e017
Michilli, D., Hessels, J. W. T., Donner, J. Y., et al. 2018, MNRAS, 476, 2704
Noutsos, A., Sobey, C., Kondratiev, V. I., et al. 2015, A&A, 576, A62
Osłowski, S., van Straten, W., Hobbs, G. B., Bailes, M., & Demorest, P. 2011, MNRAS, 418, 1258
Pennucci, T. T. 2015, PhD thesis, Univ. Virginia
Pennucci, T. T., Demorest, P. B., & Ransom, S. M. 2014, ApJ, 790, 93
Petroff, E., Keith, M. J., Johnston, S., van Straten, W., & Shannon, R. M. 2013, MNRAS, 435, 1610
Phillips, J. A., & Wolszczan, A. 1991, ApJL, 382, L27
Phillips, J. A., & Wolszczan, A. 1992, ApJ, 385, 273
Ramachandran, R., Demorest, P., Backer, D. C., Cognard, I., & Lommen, A. 2006, ApJ, 645, 303
Rankin, J. M., & Roberts, J. A. 1971, in IAU Symp. 46, The Crab Nebula, ed. R. D. Davies & F. Graham-Smith (Dordrecht: Reidel), 114
Rickett, B. J. 1990, ARA&A, 28, 561
Roberts, J. A., & Ables, J. G. 1982, MNRAS, 201, 1119

Romani, R. W., Blandford, R. D., & Cordes, J. M. 1987, Natur, 328, 324
Savitzky, A., & Golay, M. J. E. 1964, AnaCh, 36, 1627
Shannon, R. M., & Cordes, J. M. 2010, ApJ, 725, 1607
Shannon, R. M., & Cordes, J. M. 2017, MNRAS, 464, 2075
Shannon, R. M., Osłowski, S., Dai, S., et al. 2014, MNRAS, 443, 1463
Spangler, S. R., Kavars, D. W., Kortenkamp, P. S., et al. 2002, A&A, 384, 654
Stairs, I. H. 2002, in ASP Conf. Ser. 278, Single-Dish Radio Astronomy: Techniques and Applications, ed. S. Stanimirovic et al. (San Francisco, CA: ASP), 251
Stinebring, D. R., Cordes, J. M., Rankin, J. M., Weisberg, J. M., & Boriakoff, V. 1984, ApJS, 55, 247
Stinebring, D. R., McLaughlin, M. A., Cordes, J. M., et al. 2001, ApJL, 549, L97
Taylor, J. H. 1992, RSPTA, 341, 117
Verbiest, J. P. W., Lentati, L., Hobbs, G., et al. 2016, MNRAS, 458, 1267
You, X. P., Hobbs, G., Coles, W. A., et al. 2007a, MNRAS, 378, 493
You, X. P., Hobbs, G. B., Coles, W. A., Manchester, R. N., & Han, J. L. 2007b, ApJ, 671, 907